Optical Materials 36 (2014) 936–940

Contents lists available at ScienceDirect

Optical Materials

journal homepage: www.elsevier.com/locate/optmat

A 2D μ-Raman analysis of low repetition rate femto-waveguides in lithium niobate by using a finite element model

M.R. Tejerina [a,*], D. Jaque [b], G.A. Torchia [a]

[a] Centro de Investigaciones Ópticas CONICET La Plata CIC, Camino Centenario y 506 s/n M.B. Gonnet (1897), Pcia Buenos Aires, Argentina
[b] Departamento de Física de Materiales, Facultad de Ciencias C4, Universidad Autónoma de Madrid, Campus de Cantoblanco, 28049 Madrid, Spain

ARTICLE INFO

Article history:
Received 2 October 2013
Received in revised form 15 November 2013
Accepted 26 December 2013
Available online 20 January 2014

Keywords:
Lithium niobate
Femtosecond laser written optical waveguides
Raman shift mapping
Refractive index field
Residual strain field

ABSTRACT

We present a μ-Raman two-dimensional analysis of 1 kHz femtosecond laser written waveguides in an x-cut lithium niobate crystal. At first, the fitting between a two-dimensional elastic model and experimental micro Raman spectroscopy data (MR) were examined to validate the numerical model. In this, the Raman Potential Deformation Theory (RPDT) was employed to fit the wavenumber shift of the $A_1(TO)_4$ phonon. Then, the adequate values for geometrical parameters of the numerical model (horizontal and vertical ellipse radius) were estimated. Finally, using these parameter values, the guided modes were computed for different ellipse expansions and compared with experimental guided modes.

1. Introduction

Since 1996, ultra-fast (pulses of hundreds of femtoseconds) laser writing has emerged as an important tool for optical circuit fabrication. These guiding structures are essential for technological applications in the field of optical communications in terms of developing integrated components, amplifiers, and lasers, inter alia [1]. The main advantage of this fabrication method is that it can be applied to an unlimited number of optical materials. The nonlinear absorption as a consequence of there being many infrared photons in the focused region and the later micro-explosion and re-solidification are the key to obtaining a suitable material modification [1].

Due to the high complexity of the nonlinear interaction, the generation of waveguides using different processing parameters (velocity, pulse duration and pulse energy) arose as an empirical way of improving ultra-fast laser writing [1–3]. As a result, a large number of successful integrated guiding structures have been reported by using low repetition rate laser processing (1 kHz) [4–8].

Knowledge about femto-waveguides (femtosecond laser written waveguides) origin get mainly increased because of the qualitatively comparison between experimental guided regions in them and a numerical elastic model [9–12]. This model consists of an anisotropic domain where an ellipse statically expands, and the residual mechanical deformation generates, via the piezo-optic effect, the refractive index increment necessary for wave guiding [13].

Subsequently, the wavenumber shifts of Raman $A_1(TO)$ phonons within a linear path across low repetition femto-waveguides was qualitatively reported and attributed to residual strain by Ródenas et al. [14]. Following the mentioned assumptions and merging them with the previously reported numerical model, we had quantitative analyzed Raman shifts (using the Deformation Potential Theory) in a previous work [15]. In this, the Raman scanning was taken in a linear path across the femto-waveguide and allowed, in a first approximation, the computing of the residual strain field, but only in a linear path. A quantitative two-dimensional description of the material structure in the femto-waveguide (laser-material interaction leading region) is very important when designing photonic circuits formed by this kind of waveguides because the deformation field is closely tied to the refractive index field by the piezo-optic relation [15]. In this sense, in order to extend the one-dimensional approach [15], the current work deals with a two-dimensional Raman and optical analysis of a femto-waveguide and includes the following targets: (i) validating a numerical model which hypothetically explains the two-dimensional Raman behavior; (ii) estimating the adequate values for the model geometrical parameters (horizontal and vertical ellipse radii); and (iii) using the obtained geometrical parameters values to compute the guided modes for different expansions and compare them with experimentally measured guided light.

* Corresponding author. Tel.: +54 2214840280; fax: +54 2214712771.
E-mail address: matiast@ciop.unlp.edu.ar (M.R. Tejerina).

0925-3467/$ - see front matter © 2014 Elsevier B.V. All rights reserved.
http://dx.doi.org/10.1016/j.optmat.2013.12.040

2. Materials and experimental methods

2.1. Sample characteristics, femtosecond laser processing and waveguide optical coupling

The waveguide analyzed in this work was performed in an Nd:Mg:$LiNbO_3$ x-cut sample. The Nd- and Mg-doping ratios were 0.3% and 5%, respectively. The structural modification was generated with a 796 nm Ti: Sapphire ultrafast laser. The duration of the pulses was 120 fs with a repetition rate of 1 kHz and energy per pulse of 3 μJ. A 10 × (N.A. = 0.3) microscope objective was used to focalize the laser inside the crystal. The sample was displaced at a rate of 25 μm/s along the *y*-axis with a 0.2 μm resolution positioning stage. The structure modification performed in the crystal allowed light guidance; an optical image of the modification can be seen in Fig. 1(b). The wave-guiding zone is marked with the text "WG" and the probe laser spot above the direct modified material is marked with the text "PL" in this figure.

To perform optical coupling to the generated femto-waveguide, the well-known "end-fire" method was implemented using a standard 630 nm solid state laser [14]. So, the spatial distribution of the guided mode intensity at the waveguide output was measured by means of a standard Newport beam profile analyzer.

2.2. 2D μ-Raman mapping system and experimental procedure

The residual mechanical deformations in the generated waveguides were studied with back-scattering μ-Raman spectroscopy mapping with a *y*(*zz*)*y* configuration. For this mapping, a 200 mW argon laser centered at 532 nm and a Confocal Olympus BX-41 with an objective of 50 × (NA = 0.25) were used. A set of notch filters and a polarizer were used in the experiment [14]. The sample was displaced with a 0.1 μm resolution motorized station such that a 2D mapping of waveguides with *z*-direction and *x*-direction steps of 1 μm was generated. The well-known Raman spectrum for the $LiNbO_3$ *y*(*zz*)*y* configuration was measured and stored in each point of the mapping. The phonon $A_1(TO)_4$ was fitted with a Lorentzian function, and the energy shift in the analyzed zone was obtained as a 3D surface (energy variation of phonon vs. *z*-displacement vs. *x*-displacement). The scanning area (70 × 60 μm^2) corresponds to the image shown in Fig. 1(b).

3. Theory and numerical calculation

3.1. Raman Deformation Potential Theory (RDPT)

The Raman Deformation Potential Theory (RDPT) relates the mechanical deformation of crystals to the energy shift of optical phonons. Taking into account the symmetry of the $A_1(TO)_i$ phonons, this relationship can be described by [15]:

$$\Delta E_{A_1(TO)i} = e_i \times (\varepsilon_{xx} + \varepsilon_{yy}) + f_i \times (\varepsilon_{zz}) \quad (1)$$

In Eq. (1), $\Delta E_{A_1(TO)i}$ is the wavenumber shift of a "*i*" phonon of symmetry A_1(Transverse Optical); e_i and f_i are the A_1 phonon deformation potential constants; and ε_{xx}, ε_{yy} and ε_{zz} are the elements of deformation tensor.

In the current model, ε_{xx} and ε_{zz} are "surfaces" (functions of *x* and *z*) which depend on the model parameters values and ε_{yy} is equal to zero. So, Eq. (1) will turn into Eq. (2).

$$\Delta E_{A_1(TO)i} = e_i \times \varepsilon_{xx}(z,x) + f_i \times \varepsilon_{zz}(z,x) \quad (2)$$

In Eq. (2), it can be seen that the resulting strain field should be related with the Raman shift field by a linear combination.

3.2. Numerical model for strain field computing

The numerical model used in this work consists of a quarter of an ellipse which statically expands in an elastic domain. A scheme of the model is shown in Fig. 1(a). The input parameters of the model are four: the initial horizontal radius (*a*), the initial vertical radius (*b*), the horizontal expansion parameter ($\alpha = \Delta a/a$) and the vertical expansion parameter ($\beta = \Delta b/b$). In Fig. 1(a), the geometrical input parameters are shown (*a* and *b*). And the dashed line near the ellipse represents the final geometry after the static expansion (so, the "after expansion" radii are: $a + \Delta a$ and $b + \Delta b$).

This model represents an arbitrary mechanical expansion which generates a strain field in the waveguide region and therefore, a hypothetically Raman shift variation and a refractive index variation (by means of the piezo-optic effect, Eq. (4)). Physically, this expansion is the result of many linear and non-linear complex phenomena which, in general, have not been quantitatively and independently determined yet [8]. The ellipse geometry can be related, in some way, with the focal intensity distribution and the expansion represents the focal volume variation occurring after the laser-material interaction.

To compute the strain field (ε_{xx} and ε_{zz}) after the ellipse expansion, we used a code generated in MATLAB environment. This open code was published in a previous work [13] and the assumptions/approximations made in this finite element model were detailed in another work, where a linear path of Raman shift across femto-waveguides is analyzed [15]. As mentioned in the cited works, the numerical model makes the following general assumptions: elastic material, static expansion, plane strain deformations ($\varepsilon_{yy} = 0$) and orthotropic approximation for $LiNbO_3$ compliance matrix.

3.3. Method

3.3.1. Setting expansion parameters (α and β) for optimal geometrical parameters computing

In order to make a first evaluation of the model and compute the optimal geometrical parameters (*a* and *b*), we set the expansion parameters as follows, $\alpha = \beta = 0.01$. Taking into account the following:

- $\alpha = \beta$; this simplification was introduced by other authors and gave, qualitatively, a good approximation of the guided zones in femto-waveguides in $LiNbO_3$ [9].
- $\alpha = \beta = 0.01$; the scope of this work includes the estimation of the optimal values of *a* and *b* ellipse radii for the μ-Raman map fitting. The absolute value of the expansion does not, however, change the fitting error: this conclusion can be reached by analyzing Eq. (2); if the numerical expansion is increased, i.e. α and β are increased and if the relation between them is fixed,

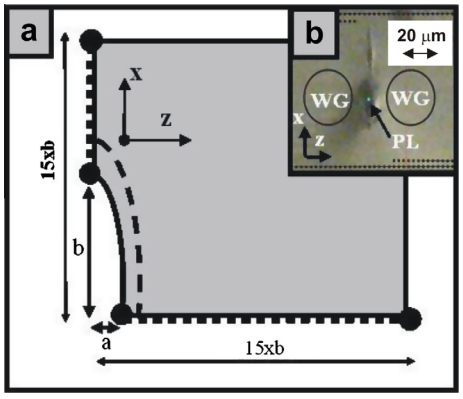

Fig. 1. (a) Finite element model domain; (b) optical microscopic image corresponding to the mapped region.

the strain fields (ε_x and ε_z) obtained after increasing α and β are proportional to those obtained before the increment. So, e and f, which are the fitting parameters, decrease to fit the experimental Raman field and the resultant Raman field and the fit error will not change. So, a value of 0.01 for α and β is set because similar values were also found in other papers [9,10].

3.3.2. Procedure

Firstly, the expansion in the numerical model (α and β) was fixed using values from literature (as explained in Section 3.3.1). Following, the corresponding strain fields (ε_{xx} and ε_{zz}) were computed for different values of a (from 0.1 to 3.2 μm) and b (from 6 to 12 μm). Then, each pair of the obtained ε_{xx} and ε_{zz} surfaces were fitted (using non-linear square error fitting of MATLAB package: "fminsearch.m") to the measured Raman shift mapping by means of Eq. (2) and using e and f as fitting parameters. Following, the Total Square Error (TSE) of each fitting (Eq. (3)) was computed and plotted for each pair of geometrical parameters (a,b) (Fig. 4). Subsequently, the different TSE were compared and the optimal values of a and b (a_o and b_o) were obtained.

$$\mathrm{TSE} = \sum_{i=1}^{n} \left(\Delta \mathrm{ATO}_{\mathrm{exp}}(z_i, x_i) - \Delta \mathrm{ATO}_{\mathrm{num}}(z_i, x_i)\right)^2 \quad (3)$$

In Eq. (3), $\Delta A_1TO_{exp}(z_i,x_i)$ is the experimental Raman shift at the coordinate (z_i,x_i), $\Delta A_1TO_{num}(z_i,x_i)$ is the numerically computed Raman shift at the coordinate (z_i,x_i).

Using the obtained optimal geometrical parameters (a_o and b_o), the guided modes were computed for different expansions values (α and β). To this end, the steps indicated by Okamoto [16] were followed. Then, the computed guided modes were compared with experimentally measured guided light.

In the zone close to the perimeter of the ellipse, plastic effects can take place because of shock waves after femtosecond interaction [3,17,18]. As a result, the elastic numerical approach is not suitable to fit this zone. Consequently, we removed from the Raman mapping domain the area enclosed by a quarter of ellipse of radii 1.4∗a and 1.4∗b to adjust the experimental results.

4. Results and discussion

4.1. The 2D μ-Raman mapping

As mentioned in Section 2.2, a map of the energy shift of the $A_1(TO)_4$ Raman phonon was obtained in low repetition rate (1 KHz) femtosecond waveguides written in a Nd:Mg:$LiNbO_3$ crystal. This field is shown in Fig. 2.

In Fig. 2, six principal lobes can be observed: although the pattern of the Raman mapping has certain symmetry, so-called "plane symmetry," (i.e. the curves which are the limits of the six lobes seem to be quasi-symmetric), it can be seen that the "intensity" of the different lobes is not symmetric. This asymmetry of the Raman shift could be generated by an asymmetric expansion during/after material-femtosecond laser interaction. Although this non-symmetry is reported by other authors [14], its origin and its main characteristics are not yet well understood.

The fact that the limits of the lobes are symmetric is in agreement with the numerical model proposed, but this does not apply to the lobes "intensity" as they are not fully symmetric. In any case, to test the numerical model and compute the optimal geometrical parameters (a and b), the four quadrants ($c1$, $c2$, $c3$, $c4$) were averaged. As a result, in Fig. 3 we present the averaged spectral shift in a quarter of the domain. Also, in Fig. 3, two main lobes can be defined: one of them through the horizontal kl path and another through the ij path. The ij lobe has a positive Raman shifts whereas the kl lobes show a negative shift.

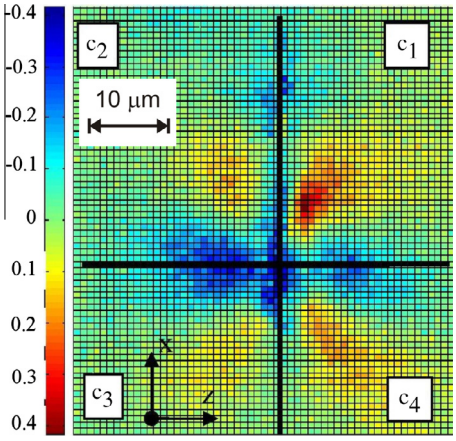

Fig. 2. Raman shift mapping of femtosecond waveguide.

4.2. Total Summation Error (TSE) of the μ-Raman fitting for different ellipse input parameters (a and b)

The wavenumber shift of phonon $A_1(TO)_4$ shown in Fig. 3 was fitted for different values of the quarter-ellipse radii, and, the TSE was determined. The result is plotted in Fig. 4.

In Fig. 4, the contour level lines show that, the optimal horizontal radius (a_o) and the optimal vertical radius (b_o) are around 1.7 μm and 8.5 μm, respectively.

In Fig. 4, it can also be seen that the value of TSE increases more slowly for values of b which are above b_o, than for those lower than b_o. This suggests that there is a lower limit for the b value, and it is equal to 8 μm.

Analyzing in the same way the behavior of TSE for the values of a, we clearly see an optimum value of a_o around 1.7 and an upper limit of a of 2 μm can be estimated because for values lower than 1.7 μm the TSE surface has a lower slope (see Fig. 4).

In sum, the computed values for a_o and b_o are 1.7 and 8.5 μm respectively, but considering the resulting TSE surface it can be stated with more certainty that the upper limit of a and the lower limit of b(b_l) are 2 μm and 8 μm respectively.

In [15], a linear Raman mapping was used to analyze a similar waveguide and the values obtained for a_o and b_o were 0.6 and 7.8 respectively. Therefore, a relatively small change (about 10%) was observed in the computed b_o parameter and a more important change was observed in the computed a_o parameter (about 60%), compared with the values computed in the current work. We think that the current result is more representative, because it

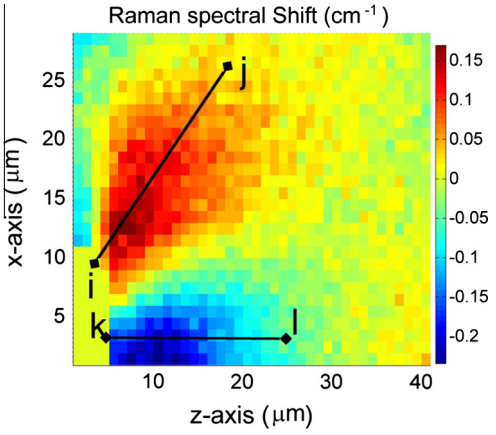

Fig. 3. A_1TO_4 relative Raman shift mapping of averaged quadrants.

corresponds to a bidimensional Raman characterization of the waveguide.

4.3. Fitted μ-Raman shift field for optimal geometrical parameters

For the optimal geometrical parameters ($a = 1.7$ μm and $b = 8.5$ μm) mentioned in Section 4.2, the resultant numerical μ-Raman field is shown in Fig. 5. This figure shows two lobes that are well defined as observed in the averaged experimental map shown in Fig. 2: a positive lobe centered along *ij* path and a negative lobe along *kl* path (see Fig. 5).

Comparing Fig. 3 with Fig. 5, it can be seen that the numerical result follows almost the same behavior as that presented in the experimental Raman mapping. The sum of the square error between them is about 1.2 and the correlation coefficient between them is about 0.9. This indicates that a good fitting is reached using the numerical model. Thus, the numerical model should be adequate to evaluate the strain field in a two-dimensional femtowaveguide zone.

4.4. Refractive index field for the obtained parameters

In this kind of waveguide, the refractive index variation which generates waveguiding is Δn_x [12], which corresponds to the ordinary refractive index component. For the used values of α and β (0.01) and using the resulting strain field and the piezo-optic expression shown in Eq. (4) [13], we computed the Δn_x residual refractive index field and it is presented in Fig. 6. It can be seen that the refractive index variation has a positive sign along the *ij* and *kl* paths, whereas the Raman shift (Fig. 5) has a positive lobe along the *ij* path and a negative lobe along the *kl* path. This suggests that the common simplification used in other works, i.e. that a positive/negative Raman shift necessarily corresponds to a positive/negative refractive index variation, is not always valid. Therefore, strictly speaking, the Raman shift field depends on: residual strain field; deformation potential constants; and the piezo-optical constants of the material. Also, in Fig. 6, in the regions where Δn_x (z, x) presents an increment (along path *ij* and *kl*), it is possible to confine x-polarized light (component in ordinary axis of the electric field). On the other hand, a large decrease in the refractive index is observed above the ellipse, so the light polarized in *x*-axis cannot be guided in this region [9,19].

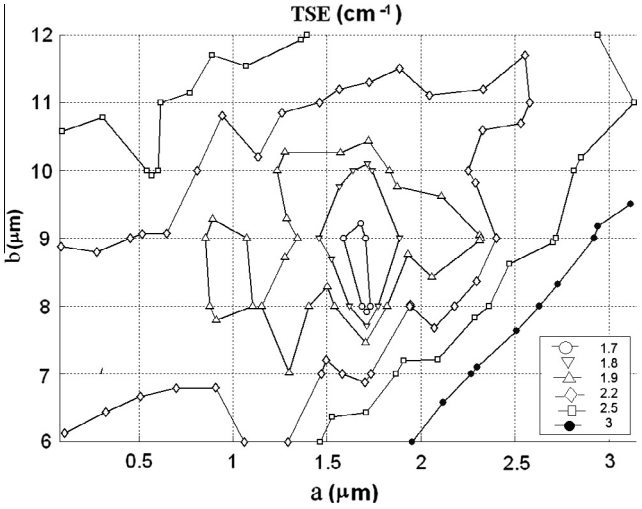

Fig. 4. Total Summation Error (TSE) as a function of different geometrical parameters (a and b).

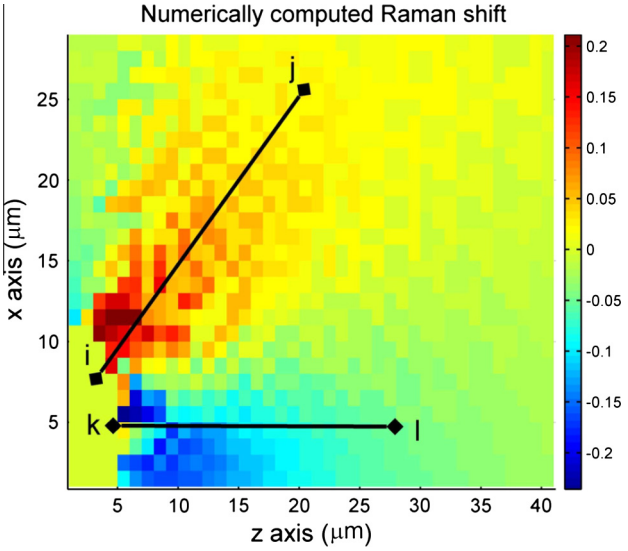

Fig. 5. Numerically computed μ-Raman shift.

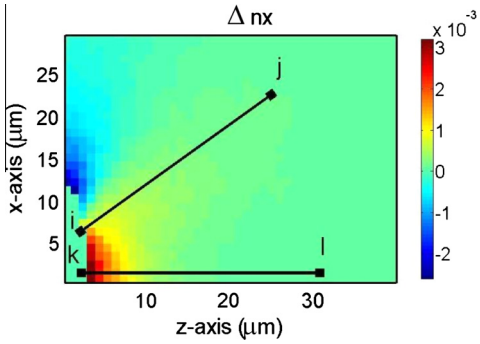

Fig. 6. Computed Δn_x field using estimated geometrical parameters ($a = 1.7$, $b = 8.5$) and $\alpha = 0.01$ and $\beta = 0.01$.

$$\Delta n_x = 0.5 \cdot n_x^3 \cdot (p_{11} \cdot \varepsilon_{xx}(z,x) + p_{13} \cdot \varepsilon_{zz}(z,x)) \quad (4)$$

In Eq. (4), p_{ij} are the *ij* strain piezo-optic elements of lithium niobate ($p_{11} = -0.026$, $p_{13} = 0.174$ and $n_x = 2.28$ were used [20]) and ε_{ij} are the *ij* elements of deformation tensor field.

4.5. Guided modes for different expansions

To evaluate the computed geometrical parameters (a_o and b_o), after computing respective refractive index field (Δn_x), guided modes were estimated following the steps indicated by Okamoto [16] for different expansion parameters (α and β). They are presented in Fig. 7(a). In this, the change experimented by the guided light when varying the expansion parameters can be observed. In Fig. 7(b), experimentally measured guided mode is shown. It can be seen that the expansion which best fit the experimental guided mode is that corresponding to $\alpha = 0.01$ and $\beta = 0$. This is enclosed by a red rectangle in Fig. 7(a) and rescaled in Fig. 7(c) for a better comparison with experimentally measured guided mode. This result reaffirms the validity of the model and the computed geometrical parameters.

5. Conclusions and future works

A two-dimensional Raman map of low repetition rate femtowaveguides in lithium niobate was presented and analyzed using

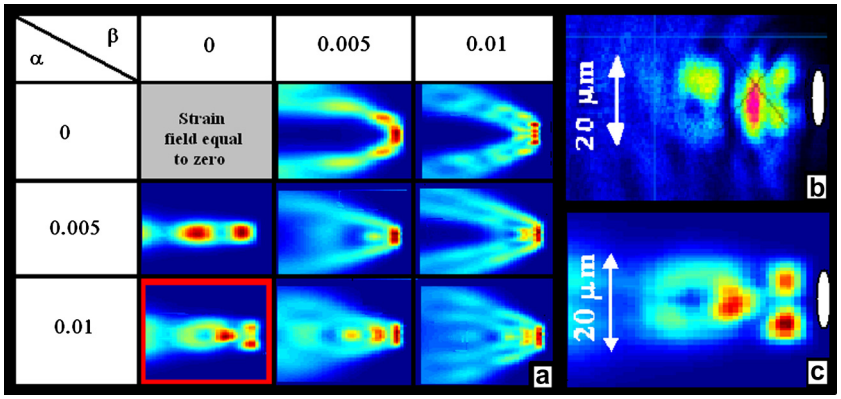

Fig. 7. Guided light in the femto-waveguide (for a wavelength of 630 nm): (a) computed modes for optimal geometrical parameters ($a = 1.7$ and $b = 8.5$) and different expansions values (α and β); (b) experimental measured guided light; (c) rescaled computed guided light which best fit experimental one, $\alpha = 0.01$ and $\beta = 0$.

an elastic finite element model. To this end, the deformation potential theory was implemented. As a result, a good correlation was obtained between the numerical model and the experimental wavenumber shift. This indicates that the model proposed explains the origin of the Raman wavenumber shifts in the two-dimensional waveguide zone. Then, the optimal geometrical parameters of the expanded area were retrieved. Following, the obtained geometrical parameters were used to compute guided modes for different ellipse expansions and these were compared with experimentally measured guided light. This comparison reaffirms good accordance between the model and the experimental measurements.

The μ-Raman two-dimensional description of the refractive index field presented in this work is the first step in the direction of a tridimensional refractive index description where conventional techniques are not suitable for use.

Furthermore, the method presented in this work can be useful to analyze, quantitatively, the Raman behavior of several optical materials under a non-hydrostatic strain field. We expect analyze this topic in future works.

Acknowledgments

This work was partially supported by the Agencia de Promoción Científica y Tecnológica under project PICT-2010-2575 and by CONICET under project PIP 5934.

References

[1] K.M. Davis, K. Miura, N. Sugimoto, K. Hirao, Opt. Lett. 21 (21) (1996) 1729–1731.
[2] C. Schaffer, PhD thesis. Harvard University, Cambridge, Massachusetts, 2001.
[3] H. Misawa, S. Juodkazis, 3D Laser Microfabrication: Principles and Applications, Wiley, VCH, Berlin, 2006.
[4] R. Gattas, PhD thesis, Harvard University, Cambridge, Massachusetts, 2006.
[5] W. Yang, PhD thesis. University of Southampton, Southampton, 2008.
[6] B. Poumellec, L. Sudrie, M. Franco, B. Prade, A. Mysyrowicz, Opt. Express 11 (9) (2003) 1070–1079.
[7] M. Richardson, A. Zoubir, C. Rivero, C. Lopez, L. Petit, K. Richardson, in: J. Neev, C.B. Schaffer, A. Ostendorf (Eds.), Micromachining Technology for Micro-Optics and Nano-Optics II Proceedings (SPIE, 2004), San Jose, CA (USA), 27–29 January 2004, vol. 5347, pp. 18–27.
[8] R. Ramponi, R. Osellame, G. Cerullo, Femtosecond laser micromachining photonic and microfluidic devices in transparent materials, Photonic Microfluidic Devices Transparent Mater. Ser.: Top. Appl. Phys. 123 (2012).
[9] J. Burghoff, S. Nolte, A. Tunnermann, Appl. Phys. A 89 (2007) 127.
[10] J. Burghoff, C. Grebing, S. Nolte, A. Tunnermann, Appl. Surf. Sci. 253 (2007) 7899.
[11] S. Nolte, J. Burghoff, M. Will, A. Tunnermann, in: J. Neev, C. B. Schaffer, A. Ostendorf (Eds.), Commercial and Biomedical Applications of Ultrafast Lasers IV Proceedings (SPIE, 2004), San Jose, CA (USA), vol. 5340, 27–29 January 2004, pp. 164–171.
[12] M. Will, J. Burghoff, S. Nolte, A. Tunnermann, in: J. Neev, C. B. Schaffer, A. Ostendorf, S. Nolte (Eds.), Commercial and Biomedical Applications of Ultrafast Lasers IV Proceedings (SPIE, 2005), San Jose, CA (USA), 24–27 January 2005, vol. 5714, pp. 261–270.
[13] M. Tejerina, G.A. Torchia, Appl. Phys. A 110 (2013) 591–594.
[14] A. Ródenas, L.M. Maestro, M.O. Ramirez, G.A. Torchia, L. Rosso, F. Chen, D. Jaque, J. Appl. Phys. 106 (2009) 013110.
[15] M.R. Tejerina, D. Jaque, G.A. Torchia, J. Appl. Phys. 112 (2012) 123108, http://dx.doi.org/10.1063/1.4769869.
[16] K. Okamoto, Fundamentals of Optical Waveguides, Elsevier, USA, 2006.
[17] E. Gamaly, Femtosecond laser-matter interactions: theory, experiments and applications, Contemp. Phys. 53 (6) (2012).
[18] M. Sokhna, PhD thesis, University of Kassel, Hessen, 2009.
[19] S.J. Beecher, R.R. Thomson, D.T. Reid, N.D. Psaila, M. Ebrahim-Zadeh, A.K. Kar1, Opt. Lett. 36 (23) (2011) 4548–4550.
[20] A.S. Andrushchak, B.G. Mytsyk, H.P. Laba, O.V. Yurkevych, I.M. Solskii, A.V. Kityk, B. Sahraoui, J. Appl. Phys. 106 (2009) 073510.